Selective N_2/H_2O Adsorption onto 2D Amphiphilic Amorphous Photocatalysts for Ambient Gas-Phase Nitrogen Fixation

Ziyang Lu[1+], Sandra Elizabeth Saji[1+], Julien Langley[1], Yunxiang Lin[2,3], Zhirun Xie[4], Ke Yang[5], Lei Bao[6], Yiyang Sun[7], Shengbai Zhang[5], Yun Hau Ng[8], Li Song[3], Nicholas Cox[1], Zongyou Yin[1]*

Dr. Z. Y. Lu, S. E. Saji, J. Langley, Assoc. Prof. N. Cox, Assoc. Prof. Z. Y. Yin
Research School of Chemistry, Australian National University, ACT 2601, Australia
E-mail: zongyou.yin@anu.edu.au

Dr. Y. X. Lin,
Institutes of Physical Science and Information Technology, Anhui University, Hefei 230601, China

Dr. Y. X. Lin, Prof. L. Song
National Synchrotron Radiation Laboratory, University of Science and Technology of China, Hefei, Anhui 230029, China

Zhirun Xie,
Particles and Catalysis Research Group, School of Chemical Engineering, The University of New South Wales, Sydney, NSW 2052, Australia

Dr. K. Yang, Prof. S. B. Zhang
Department of Physics, Applied Physics & Astronomy, Rensselaer Polytechnic Institute, Troy, NY, 12180, USA

Dr. L. Bao
Department of Chemical and Environmental Engineering, School of Engineering, RMIT University, Melbourne VIC 3000, Australia

Prof. Y. Y. Sun
State Key Laboratory of High-Performance Ceramics and Superfine Microstructure, Shanghai Institute of Ceramics, Chinese Academy of Sciences, Shanghai, 201899, China

Assoc. Prof. Yun Hau Ng
School of Energy and Environment, City University of Hong Kong, Tat Chee Avenue Kowloon, Hong Kong

[+] The two authors contributed equally to this work

Abstract

The gas-phase Haber–Bosch process has been the main industrial source of ammonia over the last century. However, its reliance on high temperature and high pressure for enormous energy input emits greenhouse gas to air and is associated with the depletion of fossil fuels. The need of the hour is to replace this method with environmentally sustainable processes, among which, photocatalytic nitrogen reduction has attracted much attention. In this work, we report a low cost, scalable manufacturing of wireless gas-phase photoreactors for nitrogen reduction under ambient conditions based on 2D amorphous molybdenum oxysulfides, i.e. MoS_{2+x}-MoO_{3-y} composites. They show excellent nitrogen reduction efficiencies of ~141 μmol/g/h with remarkably stable performance. The amphiphilic MoS_{2+x} and MoO_{3-y} composites selectively chemisorb and activate N_2 and H_2O molecules, respectively, and enable multiple photodriven redox reactions towards NH_3 evolution. Such photoreactors for ambient ammonia synthesis provides a potentially feasible route towards next-generation gas-phase industrial ammonia production.

Keywords: N2 fixation, 2D amorphous, Amphiphilic, Selective adsorption, gas-phase photocatalysis

1 Introduction

When a crystal dimension decreases to quantum/tiny scales, the enlarged surface areas increase materials utilization efficiency with receiving more local activities, which enabled various applications, including catalysis.[1] Unlike a crystal, an amorphous solid needs less energy budget for preparation and proffers rich local activities without the need of tiny size; furthermore, diverse atomic arrangements can readily form multiple amorphous solids/phases (i.e. so-called amorphous polymorphism). Amorphous bulk polymorphism was first put forward long time ago.[2] Owing to recent advancements in nanomaterials science, it has once again emerged as a promising pathway towards amorphous phase science and technology.

Many of the amorphous nanomaterials fabricated thus far exhibit good performance in catalysis, energy storage, and mechanics. Among them, two-dimensional (2D) amorphous nanomaterials have been the most attractive since they combine the merits of both 2D structure and amorphous disordering[3-6]. In catalytic applications, such 2D amorphous materials can also introduce more active sites by increasing the surface area available for catalysis in the applications such as hydrogen evolution reactions based on $Pd_3P_2S_8$[7] and on nickel monoxide,[8] and oxygen evolution reaction based on cobalt–iron hydroxide.[9] However, 2D amorphous materials for photocatalytic nitrogen reduction reaction (NRR) have been rarely reported in the literature.

Traditionally, the industrial fixation of nitrogen has been based on Haber–Bosch (HB) process which operates at high temperature and pressure. This process is responsible for 1-2% of the world's energy usage and produces hundreds of millions tons of CO_2 every year.[10] Accordingly, there is a strong push from within the international community to replace this method with environment friendly, energy efficient processes. Among these processes,

photocatalytic nitrogen reduction has gained much attention, as it imitates the natural nitrogen fixation process.[11]

However, almost all the photocatalytic NRRs reported till date operate in aqueous solution. This method has intrinsically limited-efficiency and high-costs arising from issues such as: i) reaction interruption and accelerated evaporation under N_2 gas introduction (e.g. N_2 bubbling); ii) low-temperature freezing; iii) electrolyte corrosion; iv) catalyst aggregations; and especially, (v) the low solubility of N_2 in water.[12] These limitations make a compelling case for development of gas phase NRR. Unfortunately, only few gas phase NRR systems have thus far been reported with very low efficiency, based on crystalline WO_3 synthesized at high temperature (1050-1250 ^{o}C).[13] The adsorption selectivity of N_2/H_2O molecules to amorphous NRR photocatalysts is also rarely reported.

In this work, we report the preparation of 2D amorphous molybdenum oxysulfide, i.e. MoS_{2+x}-MoO_{3-y}, composite, which uses thermal solvent synthesis followed by a relatively low temperature 200 ^{o}C annealing. It is found that the co-existence of MoS_{2+x} and MoO_{3-y} sites in amorphous MoS_{2+x}-MoO_{3-y} (a-MoS_{2+x}-MoO_{3-y}) material engenders selective adsorption to N_2 and H_2O molecules. These two sites work in concert as the active catalyst - a wireless photoreactor - to perform photo-redox NRRs in the gas-phase at ambient temperature and pressure with excellent performance stability. Significantly, the preparation of active a-MoS_{2+x}-MoO_{3-y} requires only a low thermal budget, the gas-phase wireless photoreactor is readily up-scalable, the reaction occurs at room-temperature and atmospheric pressure, and the photoinitiated reactions can be coupled to sustainable solar energy sources. All of these are crucial factors for the developments of next-generation ultra-large-scale, practical catalytic systems.

2 Experimental

Materials: Molybdenum(V) chloride ($MoCl_5$, 95%), 1-Dodecanethiol (98%), and 1-Octadecene (95%) were purchased from Sigma-Aldrich. Hexane was purchased form Chem-Supply Pty Ltd. Plain carbon cloth (1071 HCB) was purchased from The Fuel Cell Store. Water was purified by the Milli Q system. Other chemicals are all in analytic standard.

Preparation: Firstly, $MoCl_5$ (1 mmol), 1-Dodecanethiol (5 mmol) and 1-Octadecene (50 ml) were added in a 100 ml three-necked flask. A clear brown solution was obtained with the help of ultrasonication. The solution was heated to 100 °C under N_2 protection until the outcoming gas was tested to be neutral with a wet pH paper. Later, the solution was heated up to 200 °C which was maintained for 1h. The solid product was collected by centrifuge and was washed 5 times with hexane, and then dispersed in hexane.

Characterization: Transmission electron microscopic (TEM) observations were carried out on a JEOL-2100 electron microscope after the diluted dispersions of the particles were dropped onto carbon coated copper grids. The morphologies of the composites were investigated with a Zeiss UltraPlus Field emission scanning electron microscope (FESEM). X-ray diffraction (XRD) patterns were acquired on a Bruker X-ray diffractometer (Cu Ka). Atomic force microscopy (AFM) (Digital Instruments) was used to determine the thickness of the 2D composites. Photoluminescence and Raman spectroscopy were performed using a Horiba LabRAM system equipped with a confocal microscope a charge-coupled device (CCD) Si detector. The laser light with wavelength of 532 nm was focused onto the sample surface with a diameter of ≈1 μm. EPR measurements were performed using a Bruker E500 spectrometer equipped with a Bruker ER 4122 SHQE resonator. Microwave power was 0.6318 mW, microwave frequency 9.8 GHz, and modulation amplitude 5 G.

The XAFS measurements at the Mo K-edge were performed at the BL14W1 of Shanghai Synchrotron Radiation Facility (SSRF) by transmission mode. The XAFS data were analyzed by the ATHENA and ARTMIS software with FEFF code of Raval.

X-ray photoelectron spectroscopy (XPS) was employed to investigate the surface chemical bonding states of the as-prepared samples, performed on a Thermo ESCALAB250Xi X-ray photoelectron spectrometer with mono-chromated Al Kα radiation (hv=1486.6 eV) as X-ray source (power of 120 W, pass energies of 100 eV for survey scans and 20 eV for region scans, spot size 500 µm). Analysis was performed in a vacuum chamber ($<2\times10^{-9}$ mbar) and the binding energy of C 1s peak at 284.8 eV for adventitious hydrocarbon was used as a reference for calibration of all XPS results.

Property test: After washing with acetone and water, the carbon cloth was treated with Piranha solution and then washed with water several times. After that, the carbon cloth was boiled in $NaOH_{aq}$ (1 M) and then was washed in H_2SO_4 (1 M), followed by water and ethanol, and later dried in an oven. The carbon coth was cut into 1cm x 3cm pieces. The MoS_{2+x}-MoO_{3-y} hexane solution was drop casted on a carbon cloth, which was dried and then annealed in the tube furnace at defined conditions.

0.5mg of MoS_{2+x}-MoO_{3-y} drop casted per cm^2 of a carbon cloth, and a small glass vial containing 1 ml water were placed in a sealed quartz tube (Figure 3a). The quartz tube was purged with N_2 gas for half an hour and then was irradiated for 2 h under the 60 W Xe lamp. After the photoreaction, the product was collected in H_2SO_4 (1 ml, 5 mM) in a vial by purging N_2 through the quartz tube. As the water in the quartz tube may absorb the NH_3, the NH_3 concentrations in both water and H_2SO_4 were tested by the indophenol blue method. According to this method, 150 µl of a Salicylic acid, Sodium citrate, Sodium hydroxide mixture solution and 30 µl each of Sodium nitroprusside and Sodium hypochlorite were added to 3 ml of the

reaction solutions. This was kept in a shaker for 1 h for the development of colour. The reaction solutions were spectrophotometrically tested at 700 nm using a Cintra 2020 UV-Vis spectrophotometer.

Isotopic labeling: The setup for isotopic labelling studies was the same as that for NRR performance testing. 30-minute degassing was carried out for the samples sealed in the quartz bottle with ultra-high purity Argon gas and then the isotopic $^{15}N_2$ gas was flowed into the sealed quartz bottle. This bottle was then irradiated using the 60 W Xenon lamp to produce NH_3. The procedures following the reaction are mentioned in the case of NRR performance testing. The corresponding indophenol anions with ^{14}N and ^{15}N were analyzed on the Orbitrap Elite hybrid ion-trap mass spectrometer in combination with Ultimate 3000 HPLC.

DFT calculations were performed using Vienna *Ab initio* Simulation Package (VASP)[14, 15] with projector augmented wave (PAW)[16] potentials describing the interaction between ion-cores and valence electrons. Plane waves with kinetic energy cut-off of 408 eV were used as the basis set. Generalized gradient approximation of Perdew, Burke, and Ernzerhof (PBE) was used for the exchange-correlation functional[17]. Grimme's PBE+D3 method[18] was used to accurately include van der Waals interaction in the calculations. Brillouin zone was represented by the Γ point. Forces on all atoms were converged to less than 0.025 eV/Å. The amorphous molybdenum sulfide was modelled by a chain-like structure containing 6 Mo atoms and 20 S atoms, as proposed in Ref[19]. The model of amorphous molybdenum oxide was set up by a 4×4×1 supercell of bulk MoO_3. To carry out the adsorption calculation, we added a vacuum region of about 15 Å to the model. To be consistent with our experimentally measured Mo:O ratio of 1:2.8, we created the model with deficient O so that the model contained 32 Mo and 89 O atoms. The model was subject to molecular dynamics simulations at 300 K for 10 ps followed

by another 5 ps for cooling to 0 K. The time step was set to be 2 fs. The adsorption energies were calculated by taking the total energy difference with respect to molecular N_2 and H_2.

3 Results and Discussion

3.1 Material Characterization

The 2D a-MoS_{2+x}-MoO_{3-y} composites are prepared by a decomposition of coordination complex precursor ($Mo(SC_{12}H_{25})_x$) at 200 °C. After washing with hexane, the as-prepared product is further annealed at 200 °C under a vacuum of 2.5 mbar to eliminate the capping agent ($C_{12}H_{25}SH$). Scanning electron microscopy (SEM) image (**Figure 1a**) shows the as-prepared a-MoS_{2+x}-MoO_{3-y} composites have a 2D morphology with a size of several hundred nanometers. The low-temperature annealing process does not change the 2D morphology. AFM (Figure 1d) confirms the 2D morphology with thickness of ≈6 nm and shows that the composites are polydispersed with lateral size around one micron. The 2D morphology and amorphous feature are confirmed by transmission electron microscopic (TEM) (Figure 1b) and high-resolution transmission electron microscopic (HRTEM) (Figure 1c) measurements. The electron diffraction pattern shows a bright sphere without any dots or circles (inset in Figure 1c). As a comparison, the crystallized sample was obtained from annealing the sample at 400°C under the same vacuum of 2.5 mbar. Under these conditions the sample loses its 2D morphology and forms instead 1D scrolls (Figure 1e). This 2D-to-1D morphology transition is due to the mechanical stress released following formation of the crystalline structure.[20] HRTEM image with lattice fringes (Figure 1f) shows the sample attains a polycrystalline nature after annealing at 400 °C with electron diffraction data showing a dot pattern (inset in Figure 1f), in agreement with the HRTEM observation.

X-ray photoelectron spectra (XPS) measurements (Figure 1g-i) show that the material consists of both S-rich molybdenum sulfide (MoS_{2+x}) and O-deficient molybdenum oxide (MoO_{3-y}). According to previous reports, MoO_3 is generally present in amorphous MoS_{2+x}.[21] This is because adventitious water can oxidize the amorphous sheets or even react with the precursors to generate oxidized Mo clusters, thereby leading to oxide component in the amorphous composite.[21-24] For the sample annealed at 200 °C (the same temperature as that applied during thermal solvent synthesis step), Mo $3d_{5/2}$ shows three peaks at 229.41, 230.92, and 232.65eV, which correspond to Mo^{4+}, Mo^{5+}, and $Mo^{6+}(MoO_3)$ oxidation states, respectively (Figure 1g).[25] Similar to amorphous molybdenum oxysulfide thin films, Mo^{4+} ions have a trigonal prismatic environment (MoS_6) in MoS_2, the Mo^{6+} ions have an octahedral environment in MoO_3, and Mo^{5+} ions have both oxygen and sulfur neighbours.[25] Note here, we used $MoCl_5$ as the precursor for the synthesis (see experimental section). It is expected that the Mo^{5+} will be most prevalent oxidation state in the sample annealed at low temperature (200 °C), with higher temperatures suppressing the Mo^{5+} content due to loss of S. Instead, high temperature annealing should promote more MoO_3 formation due to chemisorbed water or O_2.[26]. Indeed, we found the Mo^{5+} peak dominates in the 200 °C annealed sample, but diminishes dramatically after annealing at 400 °C. The latter is accompanied by an increase in MoS_2 and MoO_3 peaks. The amorphous - crystalline phase transition occurs at 400 °C, triggering the morphology change to 1 D scrolls with 400 °C annealing.[20] In terms of S, $2p_{3/2}$, two peaks at 162.1 eV and 163. 2 eV can be observed which contribute to MoS_2 and unsaturated S^{2-}/terminal S_2^{2-} (associated with Mo^{5+} and rich S in the context), respectively, (Fig 1h).[27] Evidently, the peak at 163.2 eV decreases after annealing at 400 °C, which means the S (unsaturated S^{2-}/terminal S_2^{2-}) was lost, implying the S-rich sites related to catalysis would be affected.[27] On O 1s spectra (Figure 1i), the main peak at 531.1 eV corresponds to O^{2-} in MoO_3,[28] and peaks at

532.1 and 532.8 are attributed to oxygen vacancies and surface hydroxyl groups, respectively.[29] The oxygen vacancies peak decreased after 400°C annealing.

The amorphous and crystalline samples were further confirmed by Raman spectroscopy and powder XRD. As shown in the Raman spectrum (Figure 2a), there were no specific peaks at E^1_{2g} (375–385 cm^{-1}) and A_{1g} (400–410 cm^{-1}) for the 200 °C annealed sample. The vibration band in the 280-380 cm^{-1} region is assigned to amorphous ν(Mo-S)$_{couple}$, confirming the amorphous nature.[30] Peaks attributed to MoS_2 crystals appear at 384 cm^{-1} and 406 cm^{-1}, and are only visible in the samples annealed at 400 °C.[31] In addition, the broad peak at 825 cm^{-1} in both samples (Figure 2a) is assigned to Mo_2-O stretching modes.[32-34] In the XRD pattern, there was no specific peak of the samples annealed at 200 °C, indicating the amorphous nature of this composite (Figure 2b). However, powder XRD pattern of sample annealed at 400 °C displayed the characteristic diffraction peaks of the crystals with (100) and (110) facets of MoS_2 (Figure 2b).[35]

In the UV-Vis spectrum (Figure 2c), the black-coloured a-MoS_{2+x}-MoO_{3-y} shows a relatively broad structureless absorption. There are two absorption peaks around 260 nm and 410 nm observed after annealing at 400 °C, demonstrating the initiation of MoS_{2+x}-MoO_{3-y} crystallization.[36-38] The photoluminescence spectrum of a-MoS_{2+x}-MoO_{3-y} gives a broad peak around 680 nm from local defect states associated with oxygen vacancy of MoO_3[39] and this peak dramatically decreased after annealing at 400 °C (Figure 2d), indicating defect reduction with crystallization. Our observation is consistent with the phase transition of amorphous MoS_xCl_y prepared by CVD, using $MoCl_5$ and sulfur as precursors. Below 325 °C, only the amorphous phase could be observed. However, the material transitions to a crystalline structure when grown above 375 °C.[40] In addition, our experiment also shows that a-MoS_{2+x}-

MoO$_{3-y}$ maintains a 2D morphology and amorphous phase when they are annealed at 300 °C (Figure S1).

The MoS$_{2+x}$-MoO$_{3-y}$ phases formed under different annealing temperature is further investigated by X-ray absorption fine structure (XAFS) measurements. The X-ray absorption near edge spectra (XANES) are shown in Figure 2e for standard MoS$_2$ bulk and our composite material, which show similar features with some small difference. Characteristic peaks tend to get closer to the standard MoS$_2$ bulk with increasing temperature, indicating the similar spatial configuration of Mo after annealing. As illustrated in the Figure 2f, the absorption thresholds of 200 °C and 400 °C are higher than that of MoS$_2$ bulk, indicating a higher valence state of the Mo atom, in agreement with the aforementioned XPS results. Figure 2g shows the Fourier-transformed XAFS spectra of MoS$_{2+x}$-MoO$_{3-y}$, annealed at 200 °C and 400 °C, respectively. These compared with standard MoS$_2$ foil. The peak locates at 1.0-2.3 Å represents the interaction of Mo-S bonds while the peak locates at 2.3-3.3 Å corresponds to the Mo-Mo scattering. For the sample annealed at 200 °C, similar to an earlier report, the shorter Mo-Mo apparent bond length was observed (black arrow).[41] After annealed at 400 °C, the peak positions are similar to that of pure MoS$_2$ bulk with a lower intensity indicating the partially crystallized MoS$_2$ in these samples, which is in agreement with the Raman and XPS measurements aforementioned. The local configuration of Mo atoms for different samples is revealed through fitting the R-space spectra (Figure S2, **Table 1**). In the case of the sample annealed at 200 °C, the parameters of the Mo−S and Mo−Mo bonds are in good agreement with amorphous MoS$_{2+x}$ film as reported earlier,[42] in which the Mo-S and Mo-Mo distances were fit with 2.4 and 2.7 Å, respectively. However, the Mo-Mo distance was fit with 3.15 Å for the sample annealed at 400 °C which is similar to MoS$_2$ bulk. The short Mo-Mo distance for the sample annealed at 200 °C imply the amorphous nature of the MoS$_{2+x}$-MoO$_{3-y}$

composites, where the amorphous structure relaxes the bonding strain at short distances.[41] Moreover, as shown in Table 1, the coordination number also increases from 3.85 to 4.66 for Mo-S and from 1.63 to 3.43 for Mo-Mo after annealed at 400 °C. Unsaturated coordination environment would increase the reactivity of the catalysis.[43]

Figure 2h shows the continuous wave (CW) X-band Electron Paramagnetic Resonance (EPR) measurements of the amorphous (200 °C annealed) and crystalline (400 °C annealed) MoS_{2+x}-MoO_{3-y}. There are three signals observed: i) an intense derivative with crossing point at g=1.941; a sharp derivative signal with crossing point at g=2.004; and iii) a broad absorption feature at g=2.1, which represents the low-field edge of a signal which superimposes the more intense g=1.941 derivative. In subsequent gas exchange experiments it is shown that the g=1.941 signal is composite, made up of two axial Mo(V) signals corresponding to the two Mo environments of the material i.e. square-pyramidal Mo-S (MoS_{2+x}) and Mo-O (MoO_{3-y}).[30, 44] It is clear that the g=1.941 signal decreased to a large extent after annealed at 400 °C, in good agreement with the XPS data. The other two signals are not changed by annealing and thus are unlikely to be involved directly in catalysis. The sharp signal at 2.004 is assigned to a sulfur centered defect site, whereas the more broad underlying signal could be a assigned to a number of species i.e. an axial Mo(III)-S center, a more rhombic Mo(V) center with both S/O ligands or possibly a S centered radical/radical chain.[44-46]

3.2 Catalytic Activity

A wireless gas-phase photoreactor was assembled for NRR by loading the a-MoS_{2+x}-MoO_{3-y} composites onto carbon cloth to work as the freestanding photocatalysts, as schematically shown in Figure 3a, where photodriven NRRs were performed at ambient conditions, i.e. at room temperature and under normal pressure. After the photocatalysis reaction, the NH_3 is

detected by the indophenol blue method, where the peak at 700 nm is used to measure the NH_3 concentration in the UV-Vis spectrum i.e. NH_3 was converted to the indophenol anion form by its reaction with phenol, sodium hypochlorite and sodium nitroprusside in a basic environment. The a-MoS_{2+x}-MoO_{3-y} composites annealed at 200 °C shows much better NRR efficiency (86.2 µmol/g/h) than the sample annealed at 400 °C (6.7 µmol/g/h) (Figure 3b). This is attributed to the amorphous structure of the catalyst which is supposed to provide rich local active sites.[47] To confirm that the NH_3 formed during the photocatalytic reactions originated from the N_2, the photocatalytic reaction was conducted by using $^{15}N_2$ as the gas source. The corresponding indophenol anions with ^{14}N and ^{15}N were analyzed by liquid chromatography-mass spectrometry (LC-MS). With ^{14}N input, the indophenol anion shows the peak at m/z 198 and that of ^{15}N gives the peak at m/z 199. In Figure 3f, the product obtained by using $^{15}N_2$ as the gas source exhibited a much stronger peak at m/z 199 than that of its natural abundance, indicating that N_2 was indeed the source of NH_3 produced during the photocatalytic reactions. In order to enhance NRR efficiency further, we optimized the vacuum pressure under the optimal 200 °C annealing condition. Negative pressures during annealing facilitate removal of surface capping agents ($C_{12}H_{25}SH$) which block the catalytic reaction pathways. Furthermore, the same procedure can also perturb the S-rich structure of a-MoS_{2+x}-MoO_{3-y}, which diminishes performance due to the loss of disulfide active sites.[48, 49] Figure 3c shows the performance of the samples annealed at 200° C at different pressures. The composite annealed at 50 mbar shows the best performance producing ~141.2 µmol/g/h of product, which is comparable with most of other materials in literature, such as Cu-TiO_2 with 79 µmol/g/h, Ru-GaN with 120 µmol/g/h, and Bi_5O_7I of 223µmol/g/h NH_3 yield.[50-52] Moreover, we note that these a-MoS_{2+x}-MoO_{3-y} composites show excellent NRR photoredox catalytic stability. As

shown in Figure 3d, the amount of NH_3 increases almost linearly after prolonged photoirradiation (up to 24 hrs) by repeating 12-cycle reactions on the same photocatalyst. The stability of the catalyst is also tested with the Raman spectra. Based on the Raman results as shown in Figure S3, there is no obvious change after 40 hours of photoreaction, which implies the catalyst could be stable up to 40 hrs. However, two specific peaks at E^1_{2g} (375–385 cm^{-1}) and A_{1g} (400–410 cm^{-1}) of MoS_2 appeared after 60 hrs, indicating the structural phase transformation of amorphous MoS_{2+x} to the MoS_2 with forming some long-range ordered structure, which has also been observed in hydrogen evolution process.[53]

In the NRR process, two reactant molecules of N_2 and H_2O will be, respectively, involved in the reduction and oxidation reactions, which couple to complete N_2 fixation into ammonia. The oxide component in a-MoS_{2+x}-MoO_{3-y}, MoO_{3-y} is expected to favor H_2O molecular adsorption. The calculated adsorption energy of H_2O on $MoO_{2.8}$ is as low as -1.24 eV, much lower than that on MoS_{2+x} (-0.83 eV) (Figure 4b). The other component of the composite, S-rich amorphous MoS_{2+x}, was studied theoretically in the N_2 adsorption for a better in-depth understanding. Based on the theoretical calculations, it was found that the S-rich amorphous MoS_{2+x} shows excellent N_2 adsorption capacity due to a very low adsorption energy of just -0.84 eV (Figure 4b). This is much lower than the adsorption energy for N_2 on the amorphous $MoO_{2.8}$ (-0.49 eV) and normal crystalline MoS_2 (-0.11 eV) (Figure 4e). Furthermore, this value is lower than N_2 adsorption energies on metal doped TiO_2 and other transition metal particles.[51, 54] Such adsorption behavior manifests that the MoS_{2+x} and MoO_{3-y} components selectively chemisorb N_2 and H_2O molecules, respectively. It is worth noting here, we found our S-rich structure also influenced the wettability of the 2D a-MoS_{2+x}-MoO_{3-y}. From the contact angle measurements (Figure 4a), the MoS_{2+x}-MoO_{3-y} composites annealed at 200 °C shows a neutrally hydrophobic-hydrophilic, i.e. amphipathic, nature (contact angle of

approximately 90°), which is suitable for adsorbing both non-polar N_2 and polar H_2O molecules for NRR. The contact angle of water droplets on samples annealed at 400 °C shows that they are slightly more hydrophilic (56°) because of the loss of sulfur and more oxides formed in the samples as proven by XPS. Indeed, the interfacial amphipathic properties of the catalyst is also considered as a factor affecting the reactant adsorption and hence catalysis,[49] especially for gas phase reactions. Therefore, our a-MoS_{2+x}-MoO_{3-y} composites annealed at 200 °C show superior catalytic performance. It shows a promising scenario where the amphipathicity, as one of the important factors to determine catalyst-reactants solid-gas interface interactions, proffers a strong synergy for the photoredox reactions, thus enabling the superior NRR.

In order to further understand how the amorphous nature of MoS_{2+x} in MoS_{2+x}-MoO_{3-y} affects its photocatalytic properties, the Gibbs free energy for nitrogen fixation at different steps of the material and its corresponding crystals of MoS_2 are calculated as shown in Figure 4e.[11, 55] The amorphous structure of the MoS_{2+x} (Mo_6S_{20}) and MoO_{3-y} ($MoO_{2.8}$) components were estimated based on Mo/S and Mo/O ratios in the XPS results and by referring to the previous report[30]. The first hydrogenation step leading to N=NH* is considered the most difficult and critical step in the entire N_2 fixation process.[56] N_2 hydrogenation to N=NH* required a reaction energy of 0.35 eV for the crystalline MoS_2, while the reaction energy for first hydrogenations on the amorphous MoS_{2+x} are just 0.13 eV (Figure 4e), resulting in superior N_2 activation and fixation. Subsequent N=NH* hydrogenation to N–NH_2* required a reaction energy of only0.42 eV on the surface of amorphous MoS_{2+x}, indicating that the distal pathway can be greatly accelerated at this step on a-MoS_{2+x}-MoO_{3-y}.

3.3 Catalytic Mechanism

Based on the above observation and calculation, we proposed a catalytic reaction mechanism as shown in Figure 4f, where the Mo^{5+} in the amorphous MoS_{2+x} is the active site for N_2 adsorption and the water molecules are mainly adsorbed on MoO_3 which is a good catalyst candidate for water oxidation.[57] During the illumination, the amorphous MoS_{2+x}, working as the co-catalyst, effectively accepted photogenerated electrons leading to electro–hole pair separation on the surface of MoO_{3-y},[58, 59] where the relative energy levels are referred to in other studies.[26, 59, 60] The holes remaining on the MoO_{3-y} oxidise the water to yield molecular oxygen with the generated protons and electrons transferred to amorphous MoS_{2+x}. The latter reduce the adsorbed N_2 on the Mo^{5+} site that already lowered the activation energy of reactions (Figure 4e).

To test this mechanism, we performed CW-EPR measurements throughout the reaction cycle. We started with the sample prepared by 200°C annealing (Figure 4c, Figure S4). Exposure of the composite to the two gases in darkness leads to two different outcomes: N_2 exposure does not change the EPR signal, whereas N_2/H_2O exposure leads to the selective removal of a more structured signal with g-values: $g\perp=1.941$, $g\parallel=1.91$, consistent with literature values for MoO_3.[44] As such we interpret the $g=1.941$ signal as being composite of two Mo(V) sites: square-pyramidal Mo-O centers (MoO_{3-y}) and square pyramidal Mo-S centers (MoS_{2+x}), with the latter having a smaller g-anisotropy, consistent with literature.[44] These results are consistent with N_2 and H_2O binding at these two different Mo(V) sites: N_2 at Mo-S centers (MoS_{2+x}), H_2O at Mo-O centers (MoO_{3-y}). They also show that N_2 binding is not associated with a one-electron oxidation/reduction event at a Mo center, whereas H_2O binding is. Upon illumination, the $g=1.941$ signal doesn't significantly change, consistent with the photoredox catalytic stability of the material. Finally, it was observed that upon removal of N_2/H_2O the $g=1.941$ signal recovered (~37%, Figure S5). The same behavior is observed in the less active

sample prepared at 400 °C (Figure 4d): gas exposure of the now much smaller g=1.941 signal appears to lead to a decrease of the signal and light exposure did not significantly change the intensity of the g=1.941 signal.

Turning back to the sample prepared by 200 °C annealing, we note that two other signals: the g=2.004 defect signal and broad underlying signal did not change upon gas exposure (N_2 +H_2O) further confirming that these two species are 'spectators' and not directly involved in catalysis. This shows that the rich/unsaturated sulfurs are not the active sites for nitrogen adsorption even though their presence is correlated with catalytic activity. We suggest they may instead act to capture protons from MoO_3 after water oxidation by photoexcited holes.[61] This would contribute to the hydrogen source for N_2 reduction during NRR.

4 Conclusion

In conclusion, we show the developed novel gas-phase photoreactors based on 2D amphipathic amorphous MoS_{2+x}-MoO_{3-y} photocatalysts in this work meets the requirements for a promising NRR reactor. Its key properties are: (i) a 2D morphology with amorphous nature enables integration of high-density, local and wireless nano-photoreactors for NRR; (ii) amphipathic photocatalyst surface proffers selective adsorption to N_2 and water molecules; and (iii) synergistically structured MoS_{2+x}-MoO_{3-y} nanocomposites on free-standing carbon cloth facilitate the realization of photodriven NRR under the ambient conditions. Compared to higher-cost crystalline counterparts, this cheaper amorphous MoS_{2+x}-MoO_{3-y} composite exhibits much better NRR performance with robust stability. The achieved wireless gas-phase photoreactors for nitrogen reduction at room temperature under normal pressure from this work

paves a new avenue to develop a bias-free, practical, photocatalytic strategy for next-generation NRR applications.

Acknowledgements

Supplementary material

Supplemental material is available online

References

[1] L.C. Liu, A. Corma, Metal Catalysts for Heterogeneous Catalysis: From Single Atoms to Nanoclusters and Nanoparticles, Chem. Rev., 118 (2018) 4981-5079. https://doi.org/10.1021/acs.chemrev.7b00776.
[2] P.H. Poole, T. Grande, F. Sciortino, H.E. Stanley, C.A. Angell, Amorphous polymorphism, Comput. Mater. Sci., 4 (1995) 373-382. https://doi.org/10.1016/0927-0256(95)00044-9.
[3] X.T. Wang, W.X. Shi, Z. Jin, W.F. Huang, J. Lin, G.S. Ma, S.Z. Li, L. Guo, Remarkable SERS Activity Observed from Amorphous ZnO Nanocages, Angew. Chem.-Int. Edit., 56 (2017) 9851-9855. https://doi.org/10.1002/anie.201705187.
[4] S.K. Balasingam, A. Thirumurugan, J.S. Lee, Y. Jun, Amorphous MoSx thin-film-coated carbon fiber paper as a 3D electrode for long cycle life symmetric supercapacitors, Nanoscale, 8 (2016) 11787-11791. https://doi.org/10.1039/c6nr01200k.
[5] T. Matsuyama, A. Hayashi, T. Ozaki, S. Mori, M. Tatsumisago, Electrochemical properties of all-solid-state lithium batteries with amorphous MoS3 electrodes prepared by mechanical milling, J. Mater. Chem. A, 3 (2015) 14142-14147. https://doi.org/10.1039/c5ta02263k.
[6] Z.Y. Lu, G.P. Neupane, G.H. Jia, H.T. Zhao, D.C. Qi, Y.P. Du, Y.R. Lu, Z.Y. Yin, 2D Materials Based on Main Group Element Compounds: Phases, Synthesis, Characterization, and Applications, Adv. Funct. Mater., 30 2001127. https://doi.org/10.1002/adfm.202001127.
[7] X. Zhang, Z.M. Luo, P. Yu, Y.Q. Cai, Y.H. Du, D.X. Wu, S. Gao, C.L. Tan, Z. Li, M.Q. Ren, T. Osipowicz, S.M. Chen, Z. Jiang, J. Li, Y. Huang, J. Yang, Y. Chen, C.Y. Ang, Y.L. Zhao, P. Wang, L. Song, X.J. Wu, Z. Liu, A. Borgna, H. Zhang, Lithiation-induced amorphization of Pd3P2S8 for highly efficient hydrogen evolution, Nat. Catal., 1 (2018) 460-468. https://doi.org/10.1038/s41929-018-0072-y.
[8] Z.Y. Lin, C. Du, B. Yan, C.X. Wang, G.W. Yang, Two-dimensional amorphous NiO as a plasmonic photocatalyst for solar H-2 evolution, Nat. Commun., 9 (2018) 4036 https://doi.org/10.1038/s41467-018-06456-y.

[9] W. Liu, H. Liu, L.N. Dang, H.X. Zhang, X.L. Wu, B. Yang, Z.J. Li, X.W. Zhang, L.C. Lei, S. Jin, Amorphous Cobalt-Iron Hydroxide Nanosheet Electrocatalyst for Efficient Electrochemical and Photo-Electrochemical Oxygen Evolution, Adv. Funct. Mater., 27 (2017) 1603904. https://doi.org/10.1002/adfm.201603904.

[10] R.F. Service, New recipe produces ammonia from air, water, and sunlight, Science, 345 (2014) 610-610. https://doi.org/10.1126/science.345.6197.610.

[11] X.Z. Chen, N. Li, Z.Z. Kong, W.J. Ong, X.J. Zhao, Photocatalytic fixation of nitrogen to ammonia: state-of-the-art advancements and future prospects, Mater. Horizons, 5 (2018) 9-27. https://doi.org/10.1039/c7mh00557a.

[12] M. Ali, F.L. Zhou, K. Chen, C. Kotzur, C.L. Xiao, L. Bourgeois, X.Y. Zhang, D.R. MacFarlane, Nanostructured photoelectrochemical solar cell for nitrogen reduction using plasmon-enhanced black silicon, Nat. Commun., 7 (2016) 11335. https://doi.org/10.1038/ncomms11335.

[13] E. Endoh, J.K. Leland, A.J. Bard, Heterogeneous photoreduction of nitrogen to ammonia on tungsten oxide, J. Phys. Chem., 90 (1986) 6223-6226. https://doi.org/10.1021/j100281a031.

[14] G. Kresse, J. Furthmuller, Efficiency of ab-initio total energy calculations for metals and semiconductors using a plane-wave basis set, Comput. Mater. Sci., 6 (1996) 15-50. https://doi.org/10.1016/0927-0256(96)00008-0.

[15] G. Kresse, J. Furthmuller, Efficient iterative schemes for ab initio total-energy calculations using a plane-wave basis set, Phys. Rev. B, 54 (1996) 11169-11186. https://doi.org/10.1103/PhysRevB.54.11169.

[16] P.E. Blochl, PROJECTOR AUGMENTED-WAVE METHOD, Phys. Rev. B, 50 (1994) 17953-17979. https://doi.org/10.1103/PhysRevB.50.17953.

[17] J.P. Perdew, A. Ruzsinszky, G.I. Csonka, O.A. Vydrov, G.E. Scuseria, L.A. Constantin, X.L. Zhou, K. Burke, Restoring the density-gradient expansion for exchange in solids and surfaces, Phys. Rev. Lett., 100 (2008) 4. https://doi.org/10.1103/PhysRevLett.100.136406.

[18] S. Grimme, J. Antony, S. Ehrlich, H. Krieg, A consistent and accurate ab initio parametrization of density functional dispersion correction (DFT-D) for the 94 elements H-Pu, J. Chem. Phys., 132 (2010) 19. https://doi.org/10.1063/1.3382344.

[19] P.D. Tran, Thu V. Tran, M. Orio, S. Torelli, Q.D. Truong, K. Nayuki, Y. Sasaki, Sing Y. Chiam, R. Yi, I. Honma, J. Barber, V. Artero, Coordination polymer structure and revisited hydrogen evolution catalytic mechanism for amorphous molybdenum sulfide, 15 (2016) 640. https://doi.org/10.1038/nmat4588 https://www.nature.com/articles/nmat4588#supplementary-information.

[20] X.M.S. Chu, D.O. Li, A.A. Green, Q.H. Wang, Formation of MoO3 and WO3 nanoscrolls from MoS2 and WS2 with atmospheric air plasma, J. Mater. Chem. C, 5 (2017) 11301-11309. https://doi.org/10.1039/c7tc02867a.

[21] B. Li, L. Jiang, X. Li, Z.H. Cheng, P. Ran, P. Zuo, L.T. Qu, J.T. Zhang, Y.F. Lu, Controllable Synthesis of Nanosized Amorphous MoSx Using Temporally Shaped Femtosecond Laser for Highly Efficient Electrochemical Hydrogen Production, Adv. Funct. Mater., 29 (2019) 1806229. https://doi.org/10.1002/adfm.201806229.

[22] B. Mahler, V. Hoepfner, K. Liao, G.A. Ozin, Colloidal Synthesis of 1T-WS2 and 2H-WS2 Nanosheets: Applications for Photocatalytic Hydrogen Evolution, J. Am. Chem. Soc., 136 (2014) 14121-14127. https://doi.org/10.1021/ja506261t.

[23] S.K. Park, J.K. Kim, Y.C. Kang, Amorphous Molybdenum Sulfide on Three-Dimensional Hierarchical Hollow Microspheres Comprising Bamboo-like N-Doped Carbon Nanotubes as a Highly Active Hydrogen Evolution Reaction Catalyst, ACS Sustain. Chem. Eng., 6 (2018) 12706-12715. https://doi.org/10.1021/acssuschemeng.8b01843.

[24] K.E. Lee, S.P. Sasikala, H.J. Lee, G.Y. Lee, S.H. Koo, T. Yun, H.J. Jung, I. Kim, S.O. Kim, Amorphous Molybdenum Sulfide Deposited Graphene Liquid Crystalline Fiber for Hydrogen Evolution Reaction Catalysis, Part. Part. Syst. Charact., 34 (2017) 1600375. https://doi.org/10.1002/ppsc.201600375.

[25] L. Benoist, D. Gonbeau, G. Pfister-Guillouzo, E. Schmidt, G. Meunier, A. Levasseur, X-ray photoelectron spectroscopy characterization of amorphous molybdenum oxysulfide thin films, 258 (1995) 110-114. https://doi.org/https://doi.org/10.1016/0040-6090(94)06383-4.

[26] Z.Y. Yin, X. Zhang, Y.Q. Cai, J.Z. Chen, J.I. Wong, Y.Y. Tay, J.W. Chai, J.M.T. Wu, Z.Y. Zeng, B. Zheng, H.Y. Yang, H. Zhang, Preparation of MoS2-MoO3 Hybrid Nanomaterials for Light-Emitting Diodes, Angew. Chem.-Int. Edit., 53 (2014) 12560-12565. https://doi.org/10.1002/anie.201402935.

[27] Z.Q. Liu, X.M. Zhang, B. Wang, M. Xia, S.Y. Gao, X.Y. Liu, A. Zavabeti, J.Z. Ou, K. Kalantar-Zadeh, Y.C. Wang, Amorphous MoSx-Coated TiO2 Nanotube Arrays for Enhanced Electrocatalytic Hydrogen Evolution Reaction, J. Phys. Chem. C, 122 (2018) 12589-12597. https://doi.org/10.1021/acs.jpcc.8b01678.

[28] Z. Luo, R. Miao, T.D. Huan, I.M. Mosa, A.S. Poyraz, W. Zhong, J.E. Cloud, D.A. Kriz, S. Thanneeru, J.K. He, Y.S. Zhang, R. Ramprasad, S.L. Suib, Mesoporous MoO3-x Material as an Efficient Electrocatalyst for Hydrogen Evolution Reactions, Adv. Energy Mater., 6 (2016) 1600528. https://doi.org/10.1002/aenm.201600528.

[29] L.Y. Huang, F. Zhang, Y.P. Li, H. Wang, Q. Wang, C.B. Wang, H. Xu, H.M. Li, Chemical reduction implanted oxygen vacancy on the surface of 1D MoO3-x/g-C3N4 composite for boosted LED light-driven photoactivity, J. Mater. Sci., 54 (2019) 5343-5358. https://doi.org/10.1007/s10853-018-03227-4.

[30] P.D. Tran, T.V. Tran, M. Orio, S. Torelli, Q.D. Truong, K. Nayuki, Y. Sasaki, S.Y. Chiam, R. Yi, I. Honma, J. Barber, V. Artero, Coordination polymer structure and revisited hydrogen evolution catalytic mechanism for amorphous molybdenum sulfide, Nat. Mater., 15 (2016) 640-646. https://doi.org/10.1038/nmat4588.

[31] M. Boukhicha, M. Calandra, M.A. Measson, O. Lancry, A. Shukla, Anharmonic phonons in few-layer MoS2: Raman spectroscopy of ultralow energy compression and shear modes, Phys. Rev. B, 87 (2013) 195316. https://doi.org/10.1103/PhysRevB.87.195316.

[32] M. Dieterle, G. Weinberg, G. Mestl, Raman spectroscopy of molybdenum oxides - Part I. Structural characterization of oxygen defects in MoO3-x by DR UV/VIS, Raman spectroscopy and X-ray diffraction, Phys. Chem. Chem. Phys., 4 (2002) 812-821. https://doi.org/10.1039/b107012f.

[33] M. Dieterle, G. Mestl, Raman spectroscopy of molybdenum oxides - Part II. Resonance Raman spectroscopic characterization of the molybdenum oxides Mo4O11 and MoO2, Phys. Chem. Chem. Phys., 4 (2002) 822-826. https://doi.org/10.1039/b107046k.

[34] W. Liu, C. Li, Q. Xu, P. Yan, C. Niu, Y. Shen, P. Yuan, Y. Jia, Anderson Localization in 2D Amorphous MoO3-x Monolayers for Electrochemical Ammonia Synthesis, ChemCatChem, 11 (2019) 5412-5416. https://doi.org/10.1002/cctc.201901171.

[35] C.P. Veeramalai, F.S. Li, Y. Liu, Z.W. Xu, T.L. Guo, T.W. Kim, Enhanced field emission properties of molybdenum disulphide few layer nanosheets synthesized by hydrothermal method, Appl. Surf. Sci., 389 (2016) 1017-1022. https://doi.org/10.1016/j.apsusc.2016.08.031.

[36] J.Z. Huang, X.L. Deng, H. Wan, F.S. Chen, Y.F. Lin, X.J. Xu, R.Z. Ma, T. Sasaki, Liquid Phase Exfoliation of MoS2 Assisted by Formamide Solvothermal Treatment and Enhanced Electrocatalytic Activity Based on (H3Mo12O40P/MoS2)(n) Multilayer Structure, ACS Sustain. Chem. Eng., 6 (2018) 5227-5237. https://doi.org/10.1021/acssuschemeng.7b04873.

[37] D. Gopalakrishnan, D. Damien, M.M. Shaijumon, MoS2 Quantum Dot-Interspersed Exfoliated MoS2 Nanosheets, ACS Nano, 8 (2014) 5297-5303. https://doi.org/10.1021/nn501479e.

[38] B. Li, L. Jiang, X. Li, P. Ran, P. Zuo, A.D. Wang, L.T. Qu, Y. Zhao, Z.H. Cheng, Y.F. Lu, Preparation of Monolayer MoS2 Quantum Dots using Temporally Shaped Femtosecond Laser Ablation of Bulk MoS2 Targets in Water, Sci Rep, 7 (2017) 11182 https://doi.org/10.1038/s41598-017-10632-3.

[39] N. Illyaskutty, S. Sreedhar, G. Sanal Kumar, H. Kohler, M. Schwotzer, C. Natzeck, V.P.M. Pillai, Alteration of architecture of MoO3 nanostructures on arbitrary substrates: growth kinetics, spectroscopic and gas sensing properties, Nanoscale, 6 (2014) 13882-13894. https://doi.org/10.1039/C4NR04529G.

[40] X.W. Zhang, F. Meng, S. Mao, Q. Ding, M.J. Shearer, M.S. Faber, J.H. Chen, R.J. Hamers, S. Jin, Amorphous MoSxCly electrocatalyst supported by vertical graphene for efficient electrochemical and photoelectrochemical hydrogen generation, Energy Environ. Sci., 8 (2015) 862-868. https://doi.org/10.1039/c4ee03240c.

[41] D.H. Youn, J.W. Jang, J.Y. Kim, J.S. Jang, S.H. Choi, J.S. Lee, Fabrication of graphene-based electrode in less than a minute through hybrid microwave annealing, Sci Rep, 4 (2014) 5492. https://doi.org/10.1038/srep05492.

[42] B. Lassalle-Kaiser, D. Merki, H. Vrubel, S. Gul, V.K. Yachandra, X.L. Hu, J. Yano, Evidence from in Situ X-ray Absorption Spectroscopy for the Involvement of Terminal Disulfide in the Reduction of Protons by an Amorphous Molybdenum Sulfide Electrocatalyst, J. Am. Chem. Soc., 137 (2015) 314-321. https://doi.org/10.1021/ja510328m.

[43] J. Berwanger, S. Polesya, S. Mankovsky, H. Ebert, F.J. Giessibl, Atomically Resolved Chemical Reactivity of Small Fe Clusters, Phys. Rev. Lett., 124 (2020) 096001. https://doi.org/10.1103/PhysRevLett.124.096001.

[44] L. Busetto, A. Vaccari, G. Martini, ELECTRON-SPIN RESONANCE OF PARAMAGNETIC SPECIES AS A TOOL FOR STUDYING THE THERMAL-DECOMPOSITION OF MOLYBDENUM TRISULFIDE, J. Phys. Chem., 85 (1981) 1927-1930. https://doi.org/10.1021/j150613a030.

[45] M.M. Cosper, F. Neese, A.V. Astashkin, M.D. Carducci, A.M. Raitsimring, J.H. Enemark, Determination of the g-tensors and their orientations for cis,trans-(L-N2S2)(MoOX)-O-v (X = Cl, SCH2Ph) by single-crystal EPR spectroscopy and molecular orbital calculations, Inorg. Chem., 44 (2005) 1290-1301. https://doi.org/10.1021/ic0483850.

[46] R.A. Kinney, D.G.H. Hetterscheid, B.S. Hanna, R.R. Schrock, B.M. Hoffman, Formation of { HIPTN3N Mo(III)H}(-) by Heterolytic Cleavage of H-2 as Established by EPR and ENDOR Spectroscopy, Inorg. Chem., 49 (2010) 704-713. https://doi.org/10.1021/ic902006v.

[47] B.R. Goldsmith, B. Peters, J.K. Johnson, B.C. Gates, S.L. Scott, Beyond Ordered Materials: Understanding Catalytic Sites on Amorphous Solids, ACS Catal., 7 (2017) 7543-7557. https://doi.org/10.1021/acscatal.7b01767.

[48] O. Mabayoje, B.R. Wygant, M. Wang, Y. Liu, C.B. Mullins, Sulfur-Rich MoS6 as an Electrocatalyst for the Hydrogen Evolution Reaction, ACS Appl. Energ. Mater., 1 (2018) 4453-4458. https://doi.org/10.1021/acsaem.8b00973.

[49] T. Daeneke, N. Dahr, P. Atkin, R.M. Clark, C.J. Harrison, R. Brkljaca, N. Pillai, B.Y. Zhang, A. Zavabeti, S.J. Ippolito, K.J. Berean, J.Z. Ou, M.S. Strano, K. Kalantar-zadeh, Surface Water Dependent Properties of Sulfur-Rich Molybdenum Sulfides: Electrolyteless Gas Phase Water Splitting, ACS Nano, 11 (2017) 6782-6794. https://doi.org/10.1021/acsnano.7b01632.

[50] K. Ithisuphalap, H.G. Zhang, L. Guo, Q.G. Yang, H.P. Yang, G. Wu, Photocatalysis and Photoelectrocatalysis Methods of Nitrogen Reduction for Sustainable Ammonia Synthesis, Small Methods, 3 (2019) 20. https://doi.org/10.1002/smtd.201800352.

[51] Y.X. Zhao, Y.F. Zhao, R. Shi, B. Wang, G.I.N. Waterhouse, L.Z. Wu, C.H. Tung, T.R. Zhang, Tuning Oxygen Vacancies in Ultrathin TiO2 Nanosheets to Boost Photocatalytic Nitrogen Fixation up to 700 nm, Adv. Mater., 31 (2019) 9. https://doi.org/10.1002/adma.201806482.

[52] L. Li, Y.C. Wang, S. Vanka, X.Y. Mu, Z.T. Mi, C.J. Li, Nitrogen Photofixation over III-Nitride Nanowires Assisted by Ruthenium Clusters of Low Atomicity, Angew. Chem.-Int. Edit., 56 (2017) 8701-8705. https://doi.org/10.1002/anie.201703301.

[53] F.X. Xi, P. Bogdanoff, K. Harbauer, P. Plate, C. Holm, J. Rappich, B. Wang, X.Y. Han, R. van de Krol, S. Fiechter, Structural Transformation Identification of Sputtered Amorphous MoSX as an Efficient Hydrogen-Evolving Catalyst during Electrochemical Activation, ACS Catal., 9 (2019) 2368-2380. https://doi.org/10.1021/acscatal.8b04884.

[54] B.C. Yeo, J. Kong, D. Kim, W.A. Goddard, H.S. Park, S.S. Han, Electronic Structural Origin of the Catalytic Activity Trend of Transition Metals for Electrochemical Nitrogen Reduction, J. Phys. Chem. C, 123 (2019) 31026-31031. https://doi.org/10.1021/acs.jpcc.9b08729.

[55] L.M. Azofra, N. Li, D.R. MacFarlane, C.H. Sun, Promising prospects for 2D d(2)-d(4) M3C2 transition metal carbides (MXenes) in N-2 capture and conversion into ammonia, Energy Environ. Sci., 9 (2016) 2545-2549. https://doi.org/10.1039/c6ee01800a.

[56] S.Y. Wang, F. Ichihara, H. Pang, H. Chen, J.H. Ye, Nitrogen Fixation Reaction Derived from Nanostructured Catalytic Materials, Adv. Funct. Mater., 28 (2018) 26. https://doi.org/10.1002/adfm.201803309.

[57] L.L. Jin, X.S. Zheng, W. Liu, L.L. Cao, Y.J. Cao, T. Yao, S.Q. Wei, Integration of plasmonic and amorphous effects in MoO3-x spheres for efficient photoelectrochemical water oxidation, J. Mater. Chem. A, 5 (2017) 12022-12026. https://doi.org/10.1039/c7ta03011h.

[58] H.G. Yu, P.A. Xiao, P. Wang, J.G. Yu, Amorphous molybdenum sulfide as highly efficient electron-cocatalyst for enhanced photocatalytic H-2 evolution, Appl. Catal. B-Environ., 193 (2016) 217-225. https://doi.org/10.1016/j.apcatb.2016.04.028.

[59] Y.G. Lei, J.H. Hou, F. Wang, X.H. Ma, Z.L. Jin, J. Xu, S.X. Min, Boosting the catalytic performance of MoSx cocatalysts over CdS nanoparticles for photocatalytic H-2 evolution by Co doping via a facile photochemical route, Appl. Surf. Sci., 420 (2017) 456-464. https://doi.org/10.1016/j.apsusc.2017.05.165.

[60] L. Zhou, X. Guo, Z.H. Lin, J. Ma, J. Su, Z.S. Hu, C.F. Zhang, S.Z. Liu, J.J. Chang, Y. Hao, Interface engineering of low temperature processed all-inorganic CsPbI2Br perovskite solar cells toward PCE exceeding 14%, Nano Energy, 60 (2019) 583-590. https://doi.org/10.1016/j.nanoen.2019.03.081.

[61] L.R.L. Ting, Y.L. Deng, L. Ma, Y.J. Zhang, A.A. Peterson, B.S. Yeo, Catalytic Activities of Sulfur Atoms in Amorphous Molybdenum Sulfide for the Electrochemical Hydrogen Evolution Reaction, ACS Catal., 6 (2016) 861-867. https://doi.org/10.1021/acscatal.5b02369.
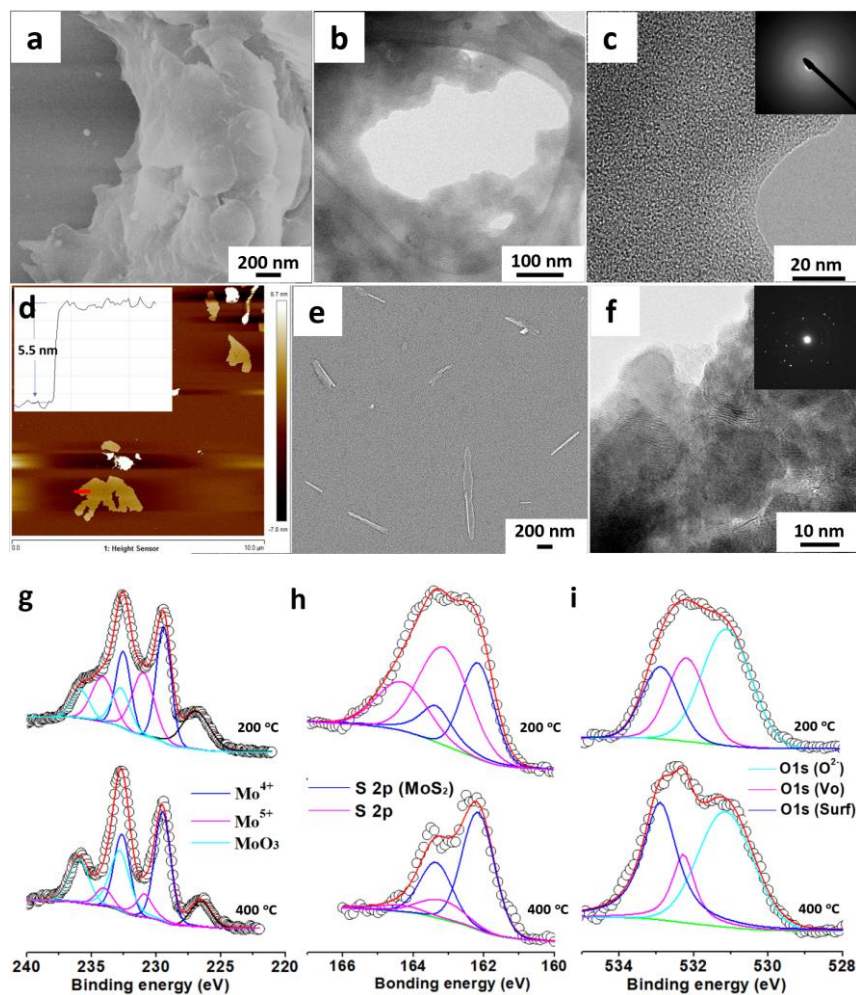
Figure 1. (a) SEM, (b, c) TEM and (d) AFM images of the a-MoS$_{2+x}$-MoO$_{3-y}$ nanosheets annealed at 200 °C and (e) SEM and (f) TEM images of the sample annealed at 400 °C. Inset images in (c) and (f) are the corresponding electron diffraction patterns, and inset in (d) is the height profile measured along the red bar on the a-MoS$_{2+x}$-MoO$_{3-y}$ nanosheet. (g) Mo 3d peaks, (h) S 2p peaks and (i) O 1s peaks in the XPS spectra of the MoS$_{2+x}$-MoO$_{3-y}$ annealed at 200 °C and 400 °C.
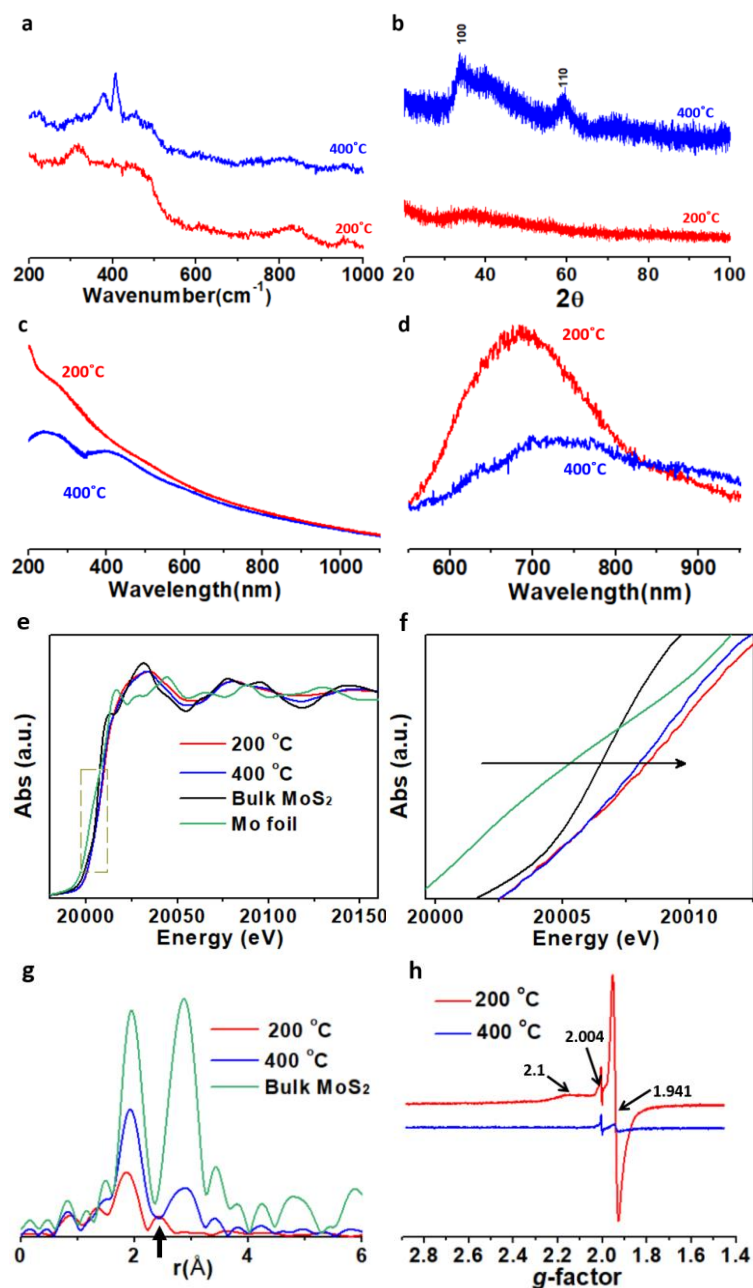
Figure 2 (a) Raman spectra, (b) XRD patterns, (c) UV-Vis and (d) photoluminescence spectra of MoS_{2+x}-MoO_{3-y} annealed at 200 °C and 400 °C. (e) Mo K-edge XANES spectra of Mo foil, bulk MoS_2 and MoS_{2+x}-MoO_{3-y} annealed at 200 °C and 400 °C, (f) is the amplified rectangle area in (e). (g) Fourier-transforms of Mo K-edge EXAFS for MoS_{2+x}-MoO_{3-y} samples annealed at different temperatures compared with the standard MoS_2 foil. (h) Room temperature EPR spectra of MoS_{2+x}-MoO_{3-y} annealed at 200 °C and 400 °C.
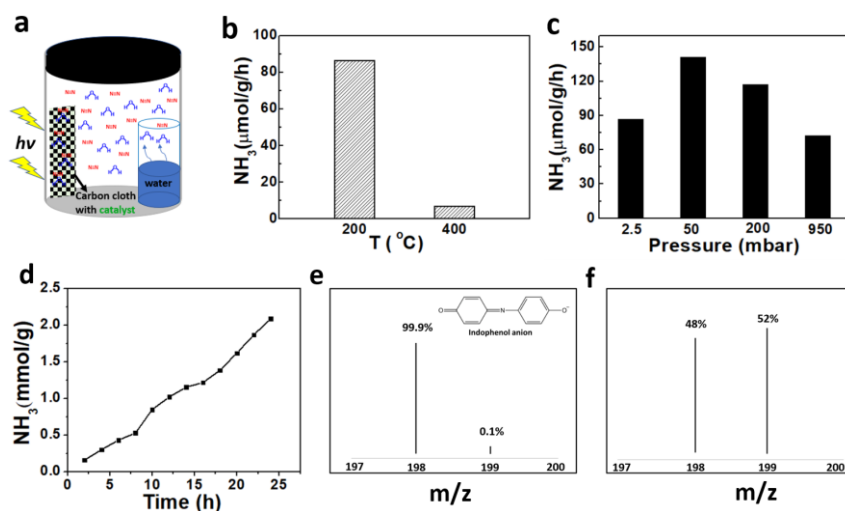
Figure 3 (a) Schematic image of a photoreactor for the gas phase NRR in which the catalyst was coated on a carbon cloth with a concentration of 0.5 mg/cm^2. Photocatalytic NRR performance of MoS$_{2+x}$-MoO$_{3-y}$ annealed at (b) 200 °C and 400 °C (under 2.5 mbar) and under (c) different pressures. (d) Amount of ammonia obtained at different reaction times for a-MoS$_{2+x}$-MoO$_{3-y}$ annealed at 200 °C. Mass spectra of the indophenols anion formed from photocatalytic ammonia products in the presence of (e) ^{14}N$_2$ and (f) ^{15}N$_2$. The inset in (e) shows the chemical structure of the indophenol anion.
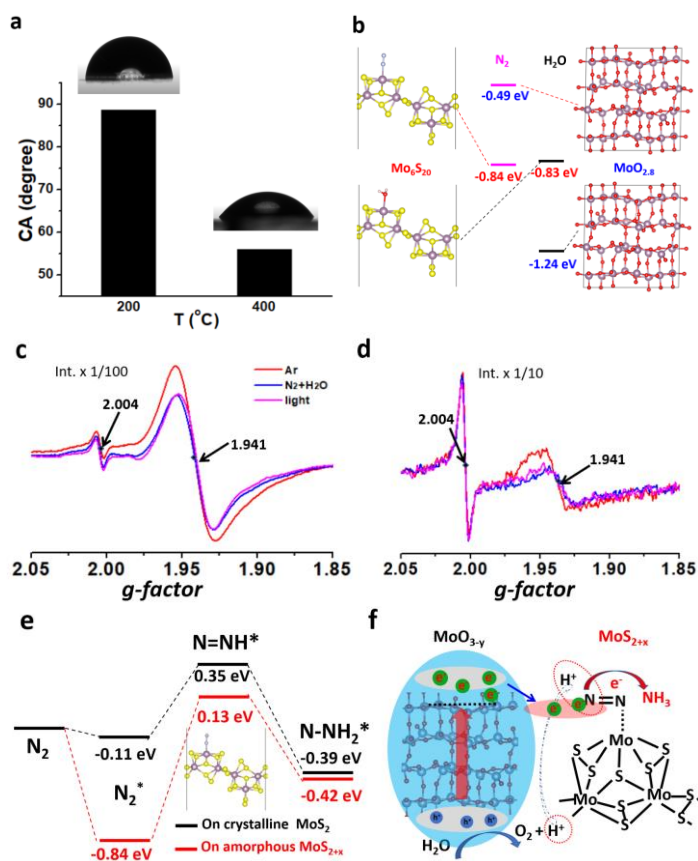
Figure 4 (a) Contact angle of water droplets on MoS_{2+x}-MoO_{3-y} annealed at 200 °C and 400 °C. (b) Calculated N_2 and H_2O adsorption energies on amorphous Mo_6S_{20} and $MoO_{2.8}$ as the sub-components in a-MoS_{2+x}-MoO_{3-y}. EPR spectrum measured on MoS_{2+x}-MoO_{3-y} annealed at (c) 200 °C and (d) 400 °C, after absorption of gaseous N_2 and H_2O, followed by illumination (intensities are divided by a factor of 100 and 10, respectively). (e) Calculated absorption energy diagram for N_2 fixation over normal crystalline MoS_2 versus amorphous Mo_6S_{20} as a sub-component in a-MoS_{2+x}-MoO_{3-y}. (f) Schematic diagram illustration of the mechanism for photocatalytic N_2 reduction reaction.

Table 1. Structural parameters calculated from Mo K-edge EXAFS fits for MoS_{2+x}-MoO_{3-y} samples annealed at 200 °C and 400 °C.

Sample	Path	N	R(Å)
MoS_2 bulk	Mo-S	6	2.41
	Mo-Mo	6	3.16
200 °C	Mo-S	3.85	2.40
	Mo-Mo	1.63	2.70
400 °C	Mo-S	4.66	2.40
	Mo-Mo	3.43	3.15

N: coordination number; R: Bond distance.